Original Article | Genitourinary Imaging

eISSN 2005-8330
https://doi.org/10.3348/kjr.2020.0121
Korean J Radiol 2021;22(1):106-117

Korean Journal of Radiology
KJR

Texture Analysis of Three-Dimensional MRI Images May Differentiate Borderline and Malignant Epithelial Ovarian Tumors

Rongping Ye, MD[1]*, Shuping Weng, MD[2]*, Yueming Li, MD[1, 3], Chuan Yan, MD[1], Jianwei Chen, MD[1], Yuemin Zhu, MD[1], Liting Wen, MD[1]

[1]Department of Radiology, The First Affiliated Hospital of Fujian Medical University, Fuzhou, China; [2]Department of Radiology, Fujian Maternity and Child Health Hospital, Fuzhou, China; [3]Key Laboratory of Radiation Biology (Fujian Medical University), Fujian Province University, Fuzhou, China

Objective: To explore the value of magnetic resonance imaging (MRI)-based whole tumor texture analysis in differentiating borderline epithelial ovarian tumors (BEOTs) from FIGO stage I/II malignant epithelial ovarian tumors (MEOTs).

Materials and Methods: A total of 88 patients with histopathologically confirmed ovarian epithelial tumors after surgical resection, including 30 BEOT and 58 MEOT patients, were divided into a training group (n = 62) and a test group (n = 26). The clinical and conventional MRI features were retrospectively reviewed. The texture features of tumors, based on T2-weighted imaging, diffusion-weighted imaging, and contrast-enhanced T1-weighted imaging, were extracted using MaZda software and the three top weighted texture features were selected by using the Random Forest algorithm. A non-texture logistic regression model in the training group was built to include those clinical and conventional MRI variables with *p* value < 0.10. Subsequently, a combined model integrating non-texture information and texture features was built for the training group. The model, evaluated using patients in the training group, was then applied to patients in the test group. Finally, receiver operating characteristic (ROC) curves were used to assess the diagnostic performance of the models.

Results: The combined model showed superior performance in categorizing BEOTs and MEOTs (sensitivity, 92.5%; specificity, 86.4%; accuracy, 90.3%; area under the ROC curve [AUC], 0.962) than the non-texture model (sensitivity, 78.3%; specificity, 84.6%; accuracy, 82.3%; AUC, 0.818). The AUCs were statistically different (*p* value = 0.038). In the test group, the AUCs, sensitivity, specificity, and accuracy were 0.840, 73.3%, 90.1%, and 80.8% when the non-texture model was used and 0.896, 75.0%, 94.0%, and 88.5% when the combined model was used.

Conclusion: MRI-based texture features combined with clinical and conventional MRI features may assist in differentitating between BEOT and FIGO stage I/II MEOT patients.

Keywords: *Borderline ovarian tumor; Malignant epithelial ovarian tumor; Magnetic resonance imaging; Texture analysis; Differential diagnosis*

INTRODUCTION

Epithelial ovarian tumors are the most common type of ovarian tumors. They account for approximately 90% of all ovarian cancers and have been recognized as the leading cause of gynecological cancer death worldwide (1).

Received: February 15, 2020 **Revised:** May 27, 2020 **Accepted:** June 1, 2020
This study has received funding by Joint Funds for the innovation of science and Technology, Fujian province (CN) (Award Number: 2019Y9125) and Special Fund of Fujian Provincial Department of Finance (CN) (Award Number: BPB-lym2019).
*These authors contributed equally to this work.
Corresponding author: Yueming Li, MD, Department of Radiology, The First Affiliated Hospital of Fujian Medical University, Key Laboratory of Radiation Biology (Fujian Medical University), Fujian Province University, Fuzhou 350005, China.
• E-mail: fjmulym@163.com

Korean Journal of Radiology
KJR

These tumors could be histologically classified into three groups, namely, benign (57–60%), borderline (4–15%), and malignant (21–33%) epithelial ovarian tumors (1). Borderline epithelial ovarian tumors (BEOTs) typically represent an intermediate grade of neoplasm between benign and malignant (1, 2) because of their specific histological features (low malignant potential and lack of stromal invasion, mitotic activity, and nuclear atypia). Due to their distinct therapeutic strategies and prognoses, it is of great importance to differentiate BEOTs from malignant epithelial ovarian tumors (MEOTs). Specifically, according to the National Comprehensive Cancer Network guidelines (Version 1.2020) (3), a conservative surgical approach with preserved fertility is recommended to treat young BEOT patients, whereas most patients with MEOTs should undergo radical surgery followed by adjuvant chemotherapy (3-5). Moreover, the prognosis of BEOT is far superior to MEOT, usually with a long-term (> 10 years) survival rate in 95% of cases (6, 7). Therefore, preoperative differential diagnosis of BEOTs and MEOTs may be crucial and helpful in determining treatment strategies and predicting the prognosis of patients with ovarian epithelial tumors.

In comparison to ultrasonography and computed tomography, magnetic resonance imaging (MRI) is a valuable tool for identifying the morphological characteristics of ovarian epithelial tumors (8). However, previous studies have revealed limitations of conventional MRI in distinguishing BEOT from MEOT, especially since these two types of tumors have very similar morphological features (9-12). Advanced MRI techniques, such as dynamic contrast-enhanced-MRI, diffusion-weighted imaging (DWI) with the measurement of the apparent diffusion coefficient (ADC), and enhanced T2*-weighted angiography, have been previously used to distinguish between the two types of tumors (13-15). Most of these studies involved a pre-selected region of interest instead of the entire tumor. This technique limits the accuracy and heterogeneity of ovarian tumors due to its large size, rendering analysis susceptible to personal selection bias and sample bias.

Texture analysis is a quantitative technique that allows the evaluation of the gray-level intensity and the relationship among pixels, which are not discernible to human eye (16). Through the assessment of gray level distribution, coarseness, and regularity in a lesion, texture analysis may be able to evaluate tumor heterogeneity based on medical images obtained in daily clinical practice. Ng et al. (17) suggested that whole tumor texture analysis could provide a more representative evaluation of tumor heterogeneity than the largest cross-sectional area analysis. To date, no study has been performed to differentiate BEOTs from MEOTs using whole tumor texture analysis. Thus, this study aimed to explore the value of MR images-based whole tumor texture analysis in differentiating BEOTs from FIGO stage I/II MEOTs.

MATERIALS AND METHODS

Participants

Patients with known or suspected history of ovarian neoplasms between September 2014 and May 2019 were retrospectively reviewed in our hospital. Patients who met the following criteria were included in the study: 1) those who preoperatively underwent standard dedicated pelvic MRI including contrast-enhanced T1-weighted imaging (CE-T1WI) and DWI; 2) those with pathologically confirmed BEOTs or MEOTs after surgical resection; 3) those with FIGO stage I/II MEOTs (tumor limited to one or both ovaries or tumor involving one or both ovaries with pelvic extension below pelvic brim or primary peritoneal cancer); and 4) those in whom the serum cancer antigen-125 (CA-125) was measured preoperatively. Patients who met the following criteria were excluded: 1) those who underwent prior related treatment (n = 10); 2) those with poor image quality due to dielectric effect artifact (n = 1); and 3) those with ruptured cystic masses (n = 3). The clinical, MRI, and pathological data recorded were reviewed. Ultimately, a total of 88 consecutive patients were enrolled for analysis, including 30 BEOT and 58 MEOT patients. Patients were then randomly allocated to either the training (n = 62) or test (n = 26) group, with the distribution of BEOTs balanced between the two groups. A flow diagram showing the patient selection protocol and the inclusion and exclusion criteria is shown in Figure 1. In cases involving peritoneal carcinomatosis, which were confined to the pelvis (FIGO stage II), we evaluated the primary lesion. In bilateral lesions, lesions with a greater solid portion or a greater septa number were selected for analysis as these radiological features suggested a more aggressive histology.

The authors are accountable for all aspects of the work in ensuring that questions related to the accuracy or integrity of any part of the work are appropriately investigated and resolved. This single-center retrospective cohort study was approved by the Institutional Review Board (No. [2016]118 and No. [2019]283), who determined the requirement for

 https://doi.org/10.3348/kjr.2020.0121

informed consent could be waived.

The datasets generated and/or analyzed during the current study are not publicly available due to patient privacy protection, but are available from the corresponding author on reasonable request.

MRI Technique

All examinations were performed using a 3T MR scanner (MAGNETOM Verio, Siemens Healthineers). The standard dedicated pelvic MRI protocol consisted of the following sequences: transverse turbo spin echo (TSE)-T1WI, transverse and sagittal TSE- T2WI with fat-suppression, and DWI (b value = 50 and 800 s/mm^2). For three phases, CE-T1WI and three-dimensional volumetric interpolated breath-hold examination with fat-suppression were performed in the transverse, sagittal, and coronal planes at 40–60 seconds, 90–110 seconds, and 170–190 seconds after intravenous injection of gadobenate dimeglumine (MultiHance, Bracco; 0.2 mmol/kg body weight; rate of 3.0 mL/s). The MRI protocol is shown in Table 1.

Conventional MRI Features Analysis

All MR images were reviewed independently by two radiologists (with 3 and 30 years of experience in abdominal MRI, respectively) who were blinded to the clinical information and the lesion type (either BEOTs or MEOTs). Similar to previous studies (18, 19), tumors were evaluated based on the following features: 1) morphology, classified as either lobulated (notches ≥ 2) or round/oval; 2) configuration, which was classified as either purely cystic, predominantly cystic (≤ 1/3 solid component), mixed cystic/solid (1/3 to 2/3 solid component), or predominantly-solid

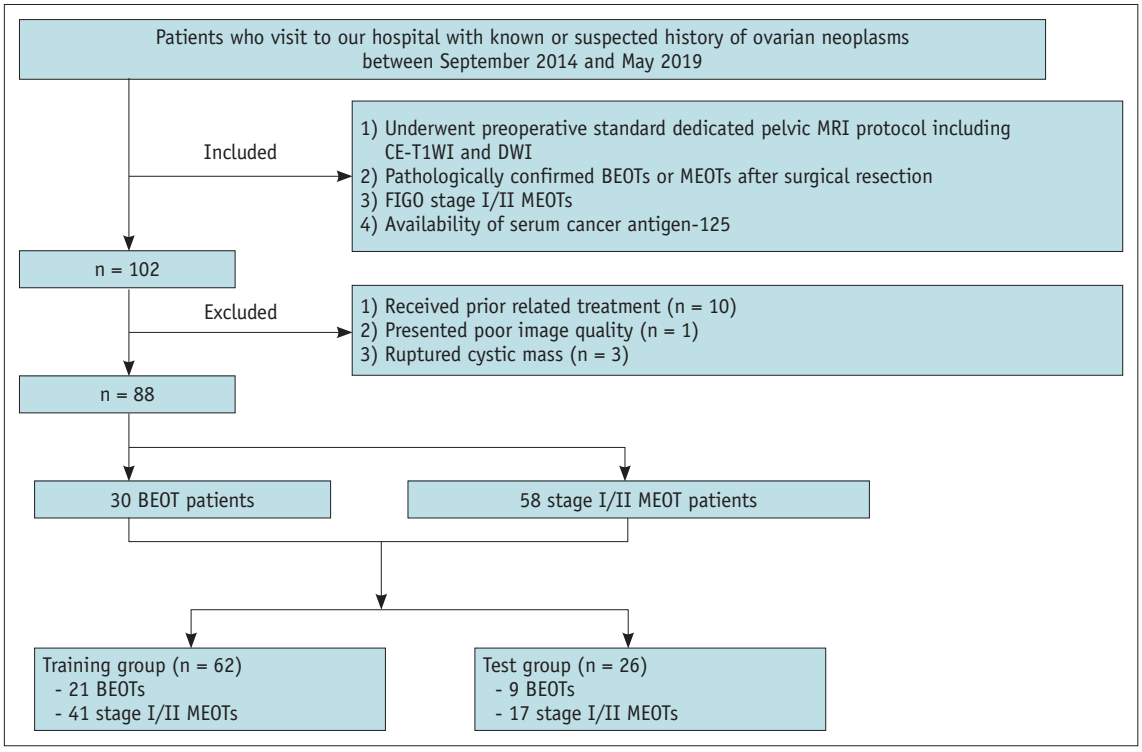

Fig. 1. Flow diagram of the inclusion and exclusion criteria for the study. BEOT = borderline epithelial ovarian tumor, CE-T1WI = contrast-enhanced T1-weighted imaging, DWI = diffusion-weighted imaging, MEOT = malignant epithelial ovarian tumor

Table 1. MRI Protocol

Sequences	TR (ms)	TE (ms)	Slice Thickness (mm)	Intersection Gap (mm)	FOV (mm)	Matrix
TSE-T1WI	800	10	5	1.0	360 x 360	384 x 384 x 70%
TSE-T2WI	4000	96	5	1.0	360 x 360	384 x 384 x 70%
DWI	6000	58	5	1.0	400 x 300	180 x 180 x 85%
VIBE-T1WI	3.2	1.2	3	0	360 x 300	384 x 384 x 70%

DWI = diffusion-weighted imaging, FOV = field of view, TE = echo time, TR = repetition time, TSE = turbo spin echo, T1WI = T1-weighted imaging, T2WI = T2-weighted imaging, VIBE = volumetric interpolated breath-hold examination

https://doi.org/10.3348/kjr.2020.0121

Korean Journal of Radiology
KJR

(≥ 2/3 solid component). Solid component was defined as a papillary projection (any enhancing solid projection into the cyst from the cyst wall with a height ≥ 3 mm) or a solid portion; 3) maximum diameter of lesion and solid component; 4) presence of thickened irregular septa defined as focal areas of septa thickening with a thickness ≥ 3 mm within a cyst (20); 5) number of loculi, classified as either unilocular, multilocular, or honeycomb loculi (grouped and innumerable sub-centimeter-sized locules) (21); 6) signal intensity, categorized as either low, moderate, or high based on the signal of the myometrium in cystic components during T1WI and T2WI; 7) the presence hemorrhagic fluid in the loculi; 8) enhancement degree of the solid component or septa/wall, categorized as either mild, moderate, or significant based on the signal of the iliopsoas and myometrium; 9) the presence of ascites, graded as either mild (limited to the Douglas pouch), moderate (limited to the pelvic cavity), or massive (beyond the pelvic); and 10) the presence of a peritoneal implant.

Image Segmentation

The sagittal T2WI, transverse DWI, and sagittal CE-T1WI images were retrieved from a picture archiving and communication system (PACS, Carestream) in Bitmap (BMP) format. The MR images were then loaded into the MaZda package for manual segmentation (open source software, http://www.eletel.p.lodz.pl/mazda/) (22). This package included image processing, extraction, and selection of texture features. To minimize the influence of contrast and brightness variation, image gray-level intensity normalization was performed using a method that normalizes image intensities within a range ($\mu - 3\delta$, $\mu + 3\delta$; μ, mean gray level value; δ, standard deviation; both μ and δ are computed separately for every volume of interest [VOI]) in MaZda. The VOI, which encompassed the whole tumor was delineated on T2WI, DWI (b value = 800 s/mm^2), and CE-T1WI images on each slice respectively segmented by the junior radiologist. ADC maps and DWI images with b values of 50 s/mm^2 were used for the segmentation of VOIs in DWI images with b values of 800 s/mm^2. The experienced radiologist validated all the segmented images. The procedure is presented in Figure 2.

Texture Feature Extraction and Selection

All 264 VOIs delineated by the junior radiologist were loaded into the MaZda package for texture analysis. The software automatically computed 314 texture features within each VOI, and generated a texture features analysis report. These texture features are shown in Table 2. Usually, only a limited number of features carry relevant information needed for texture discrimination. Therefore, texture feature reports for the training group (n = 186; 62 x 3) were loaded into the MaZda package to identify the most discriminative features for the classification of BEOTs and MEOTs. The MaZda package uses three feature selection methods: Fisher's coefficient (Fisher), classification error probability combined with average correlation coefficient (POE + ACC), and mutual information (MI). These are supervised methods (23-25). To perform feature selection based on MaZda's automatic techniques, we used a combination of Fisher, POE + ACC, and MI. Texture features with the lowest POE + ACC coefficients, the highest Fisher coefficients, and the highest individual MI were ultimately selected. Finally, thirty optimal discriminative power features from each sequence (T2WI, DWI, and CE-T1WI) of the training group were selected.

In order to solve the multicollinearity problem, the Random Forest Algorithm based on the Python Scikit-learn Library was used to select the top feature from the thirty optimal discriminative power features. It calculated the relative importance of each texture feature, and the most weighted texture features in each sequence were finally selected to construct a diagnostic model.

Statistical Analysis

Statistical analyses were performed using SPSS (version 25.0, IBM Corp.) and MedCalc (Version19.1.7, https://www.medcalc.org). The consistency of assessment between the two radiologists was evaluated by using intra-class correlation coefficients (ICC) and Cohen's kappa statistics (k) as follows: excellent (ICC/k > 0.80), good (ICC/k = 0.61–0.80), moderate (ICC/k = 0.41–0.60), and fair (ICC/k < 0.40). Numerical data were summarized using the median and interquartile range (IQR) when not normally distributed, and presented as mean and standard deviation (SD) when normally distributed. For normally distributed data, the independent sample *t* test was used, while the Mann-Whitney U-test was applied when the data are not normally distributed. Categorical variables were compared using either the Pearson's chi-squared test or Fisher's exact test.

To evaluate clinical and statistical significance, we included clinical and conventional MR variables with $p < 0.10$ to build a non-texture logistic regression model for patients

 https://doi.org/10.3348/kjr.2020.0121

in the training group. Subsequently, a combined model integrating non-texture information and texture features was built for patients in the training group. The Hosmer-Lemeshow test was applied to assess the appropriateness of fit of the two models. The model assessed in the training group was applied to the test group. The diagnostic

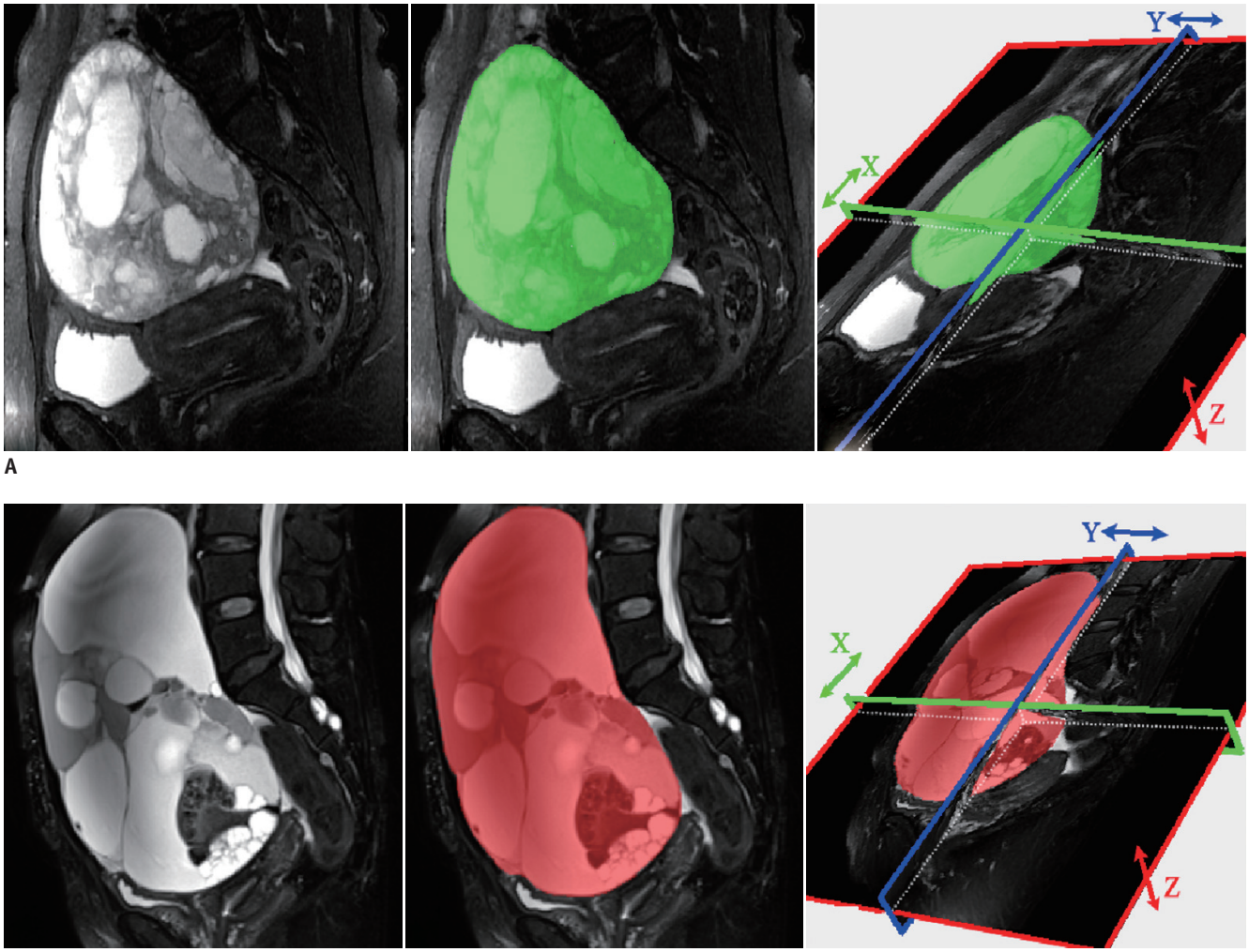

Fig. 2. T2-weighted images of patients with BEOT (A) and MEOT (B), respectively. Manually defined volume of interest was drawn layer by layer in the tumor area by the MaZda software.

Table 2. List of Texture Features in the MaZda Software

Category	More Detailed Features
Histogram (n = 9)	Mean, Variance, Skewness, Kurtosis, Perc.01%, Perc.10%, Perc.50%, Perc.90%, Perc.99%
Absolute gradient (n = 5)	GrMean, GrVariance , GrSkewness , GrKurtosis, GrNonZeros (percentage of pixels with nonzero gradient)
Run-length matrix (n = 25)	RLNonUni, GLevNonU, LngREmph, ShrtREmp, Fraction (features are computed for 5 various directions)
Co-occurrence matrix (n = 275)	AngScMom, Contrast, Correlat, SumOfSqs, InvDfMom, SumAverg, SumVarnc, SumEntrp, Entropy, DifVarnc, DifEntrp (features are computed for 5 between-pixels distances [1, 2, 3, 4, 5] and for 5 various directions)

AngScMom = angular second moment, Correlat = correlation, DifEntrp = difference entropy, DifVarnc = difference variance, GLevNonU = grey level nonuiformity, GrKurtosis = absolute gradient kurtosis, GrMean = absolute gradient mean, GrNonZeros = percentage of pixels with nonzero gradient, GrSkewness = absolute gradient skewness, GrVariance = absolute gradient variance, InvDfMom = inverse difference moment, LngREmph = long run emphsis, n = total number of texture feature of each category extracted from MaZda, RLNonUni = run length nonuniformity, ShrtREmp = short run emphsis, SumAverg = sum average, SumEntrp = sum entropy, SumOfSqs = sum of suqares, SumVarnc = sum variance

https://doi.org/10.3348/kjr.2020.0121

Korean Journal of Radiology
KJR

performance of the models and single texture features that differentiated BEOTs from MEOTs were evaluated using receiver operating characteristic (ROC) curve analysis. The areas under the ROC curve (AUCs) were analyzed using the DeLong test. A $p < 0.05$ was considered as statistically significant. However, $p < 0.10$ was selected as the filter value for univariate and multivariate analyses.

RESULTS

Clinical and Conventional MRI Characteristics

This study included 30 patients with 36 BEOTs and 58 patients with 70 FIGO stage I/II MEOTs. The gynecological symptoms or findings of patients included accidentally discovered adnexal mass (35.2%, 31/88), abdominal distension (28.4%, 25/88), lower abdominal pain (27.2%, 24/88), and abnormal uterine bleeding (9.0%, 8/88). The BEOTs included 11 serous (three bilateral cases), 18 mucinous (one bilateral case), five seromucous (one bilateral case), and two Brenner tumors (one bilateral case); whilst the MEOTs included 46 serous (12 bilateral cases), 11 mucinous, four seromucous, and nine clear cell tumors. Among the 31 MEOT patients with pathologically confirmed pelvic extension below the pelvic brim or primary peritoneal

Table 3. The Comparison of Clinical and Conventional MRI Characteristics between BEOTs and MEOTs

Characteristics	BEOT (n = 30)	MEOT (n = 58)	ICC/k*	*P*
Age, years†	46 (28.0–60.3)	52 (46.0–57.3)		0.175
Ca-125, U/mL†	30.09 (17.07–55.60)	176.80 (36.22–1041.50)		< 0.001
Morphology (%)			0.878	0.457
Lobulated	17/30 (56.7)	39/58 (67.2)		
Round/oval	13/30 (43.3)	19/58 (32.8)		
Configuration (%)			0.945	0.003
Purely cystic	1/30 (3.3)	0		
Predominantly cystic	22/30 (73.3)	22/58 (37.9)		
Mixed cystic/solid	4/30 (13.3)	18/58 (31.0)		
Predominantly solid or solid	3/30 (10.0)	18/58 (31.0)		
Maximum diameter of lesions, cm‡	15.87 ± 7.67	12.22 ± 5.40	0.861	0.101
Maximum diameter of solid component, cm‡	2.42 ± 3.68	5.27 ± 2.67	0.839	< 0.001
Thickened irregular septa (%)	15/30 (50.0)	40/58 (69.0)	0.823	0.082
Number of loculi (%)			0.895	0.127
Unilocular	6/30 (20.0)	8/58 (13.8)		
Multilocular	19/30 (63.3)	45/58 (77.6)		
Honeycomb loculi	5/30 (16.7)	3/58 (5.2)		
SI of cystic component on FS-T1WI (%)			0.927	0.439
Moderate to low	24/30 (80.0)	44/58(75.9)		
High	5/30 (16.7)	12/58(20.7)		
SI of cystic component on T2WI (%)			0.943	0.578
Low	1/30 (3.3)	3/58 (5.2)		
Moderate to high	28/30 (93.3)	53/58 (91.4)		
Enhancement (%)			0.865	0.691
Mild	6/30 (20.0)	8/58 (13.8)		
Moderate	7/30 (23.3)	17/58 (29.3)		
Significant	17/30 (56.7)	33/58 (56.9)		
Hemorrhagic fluid in the loculi (%)	4/30 (13.3)	9/58 (15.5)	0.915	0.527
Ascites (%)			0.871	0.983
No/mild	11/30 (36.7)	22/58 (37.9)		
Moderate	15/30 (50.0)	29/58 (50.0)		
Massive	4/30 (13.3)	7/58 (12.1)		

*Consistency of assessment was evaluated by ICC unless otherwise indicated, †Abnormally distributed numerical data were presented as the median (interquartile range), ‡Normally distributed numerical data were presented as the mean ± standard deviation. Consistency of assessment was evaluated by k. BEOT = borderline epithelial ovarian tumor, CA-125 = cancer antigen-125, FS = fat-suppressed, ICC = intra-class correlation coefficients, k = Cohen's kappa statistics, MEOT = malignant epithelial ovarian tumor, SI = signal intensity

https://doi.org/10.3348/kjr.2020.0121

cancer (FIGO stage II), only eight lesions (25.8%) were macroscopically observed by radiologists.

A comparison of clinical and MRI characteristics in BEOT and MEOT patients is presented in Table 3. Patients with MEOT (176.80 [36.22, 1041.50] U/mL) had higher concentrations of CA-125 (median [IQR]) than those with BEOT (30.09 [17.07, 55.60] U/mL) ($p < 0.001$). Furthermore, MEOTs had a greater solid component ($p < 0.001$) and more frequently exhibited a mixed cystic-solid or predominantly-solid configuration compared to BEOTs ($p = 0.003$) (Figs. 3, 4). Purely cystic features were only observed in BEOTs. However, there were no significant differences in other qualitative variables between the two groups.

Texture Feature Extraction and Selection

The 30 optimal texture features automatically selected by the MaZda software in the training group are shown in Table 4. Relative importance was calculated using the Random Forest Algorithm for each feature as outlined in Figure 5. The three most weighted texture features were the S(0,1,0) difference entropy (DifEntrp), extracted from T2WI images; the S(0,0,4) sum average (SumAverg), extracted from DWI images; and the S(0,0,5) SumAverg, extracted from CE-T1WI images.

Logistic Regression Models and ROC Curves

The non-texture model built in the training group included CA-125, configuration, thickened irregular septa, and maximum diameter of solid component (all p values < 0.10). The combined model built in the training group integrated non-texture information and the three most weighted texture features. Table 5 shows the performance

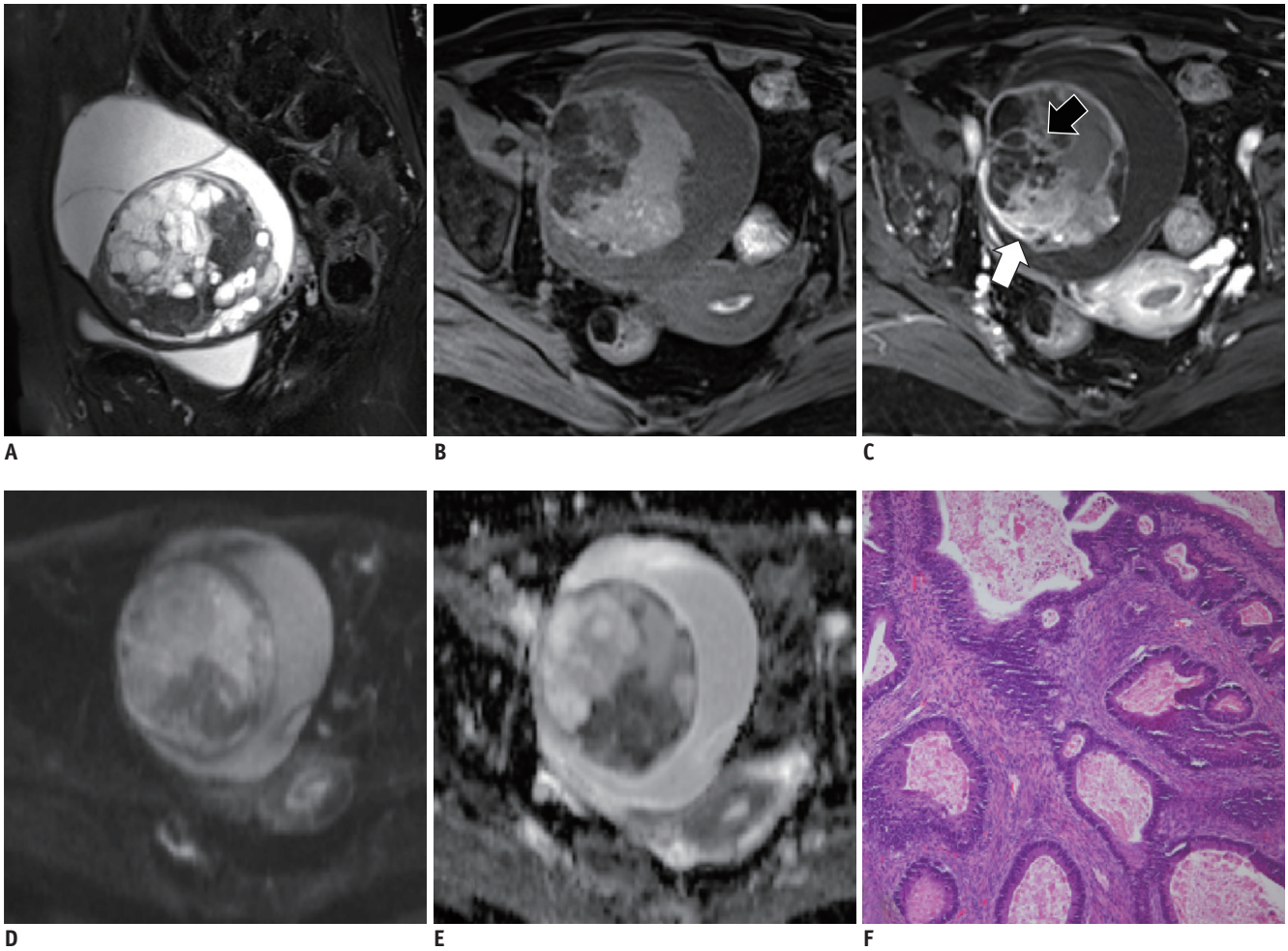

Fig. 3. A 39-year-old woman with right ovarian mucinous borderline tumor.
Sagittal T2WI **(A)** shows an oval mixed cystic-solid mass with honeycomb loculi. The cystic component exhibited low signal intensity on T1WI **(B)**. The solid component is significantly enhanced (white arrow, **C**) without restricted diffusion **(D, E)**. The septa within the tumor show irregular thickness (black arrow, **C**). The corresponding histopathological section **(F)** shows mild to moderate nuclear atypia, with stratified columnar mucin-containing cells (hematoxylin-eosin staining; magnification x 100). T2WI = T2-weighted imaging

https://doi.org/10.3348/kjr.2020.0121

Korean Journal of Radiology
KJR

of the models in differentiating BEOTs from MEOTs in the training and test groups. The Hosmer-Lemeshow test revealed that both models were predictive in differentiating BEOTs from MEOTs (p = 0.348 and 0.073, respectively). In the training group, the combined model showed a superior diagnostic performance than the non-texture model, and the comparison of AUCs revealed that the difference in diagnostic performance was statistically significant (p = 0.038). In addition, there was no significant difference in the AUCs of the combined model between the training group and the test group (p = 0.348). In the test group, however, there was no difference (p = 0.645) between the combined model (AUC, 0.896; 95% confidence interval [CI], 0.713–0.980) and the non-texture model (AUC, 0.840; 95% CI, 0.644–0.953).

The single texture features revealed a statistically significant difference between BEOTs and MEOTs in the training group (p < 0.001, p = 0.003, p = 0.015 for T2WI, DWI, and CE-T1WI images, respectively). The performance of the models and the single texture features in the training group are described in Figure 6. A comparison of

Table 4. The Frequency for Each Category of the 30 Optimal Texture Features

Category	BEOTs vs. MEOTs		
	T2WI	DWI	CE-T1WI
Histogram (n = 9)	0	0	1/30
Absolute gradient (n = 5)	3/30	1/30	1/30
Run-length matrix (n = 25)	2/30	4/30	3/30
Co-occurrence matrix (n = 275)	25/30	25/30	25/30

CE = contrast-enhanced

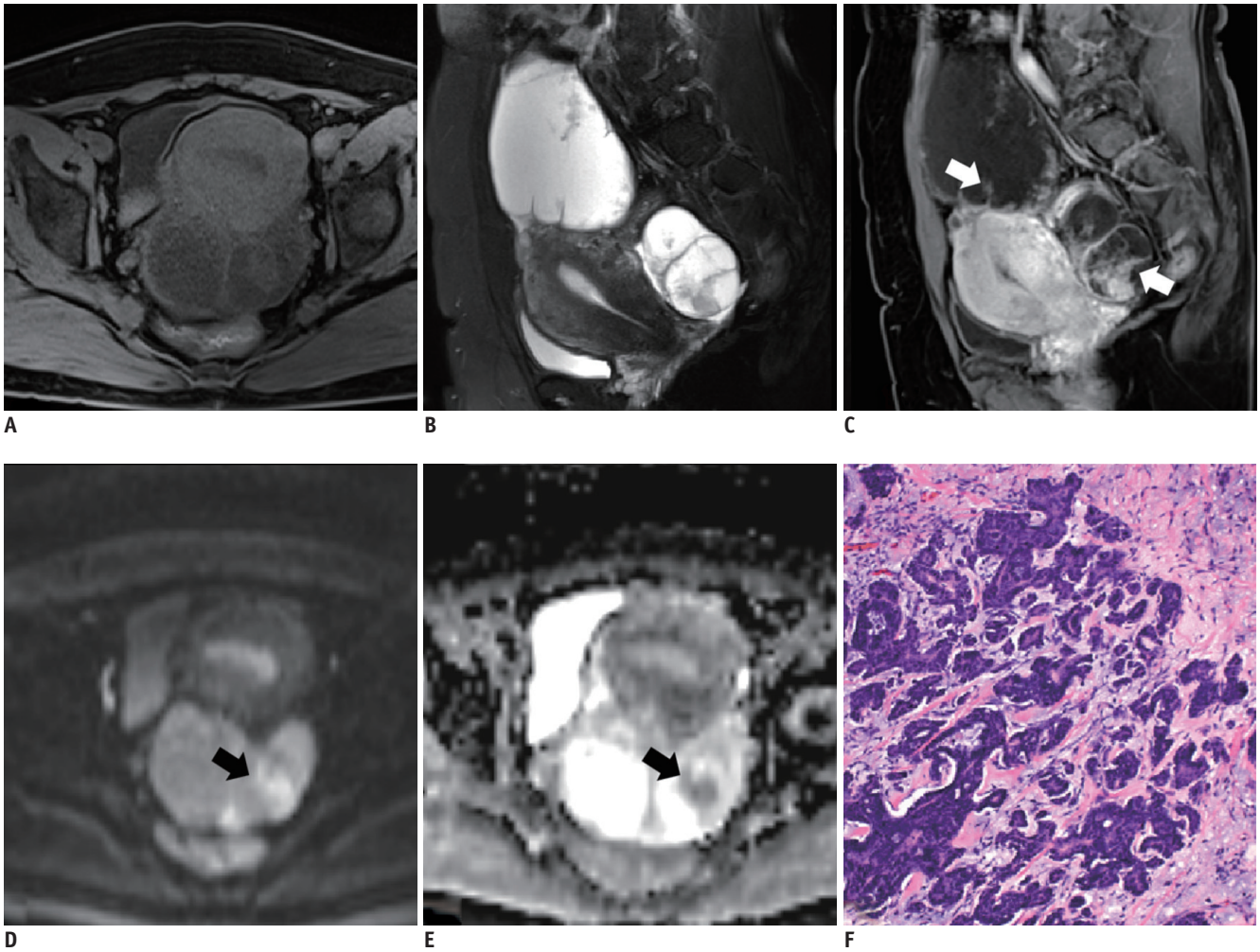

Fig. 4. A 45-year-old woman with bilateral low-grade serous carcinoma in the left fallopian tube (FIGO stage II).
Sagittal T2WI **(B)** shows cystic-predominant and mixed cystic-solid masses with thickened septas (white arrows, **C**). The solid component exhibited moderate signal intensity during T1WI **(A)** and restricted diffusion (black arrow, **D, E**). After contrast enhancing, it becomes markedly enhanced. The corresponding histopathological section **(F)** shows a solid component of cells with nuclear atypia (hematoxylin-eosin staining; magnification x 100).

https://doi.org/10.3348/kjr.2020.0121

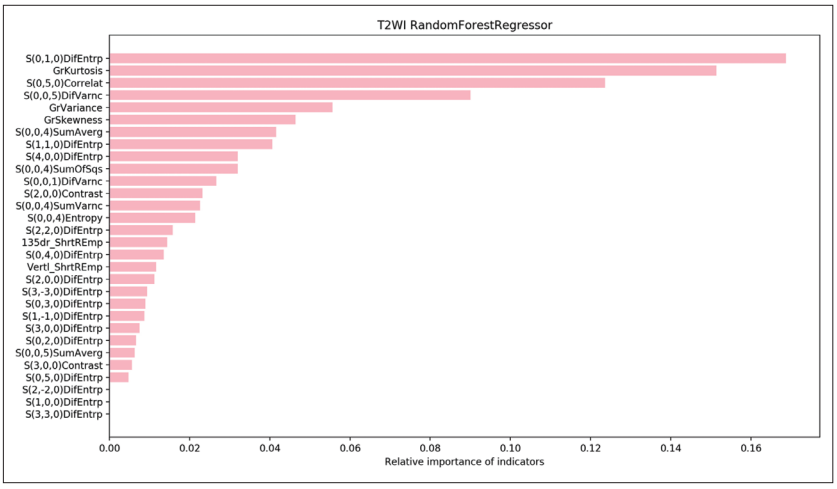

A

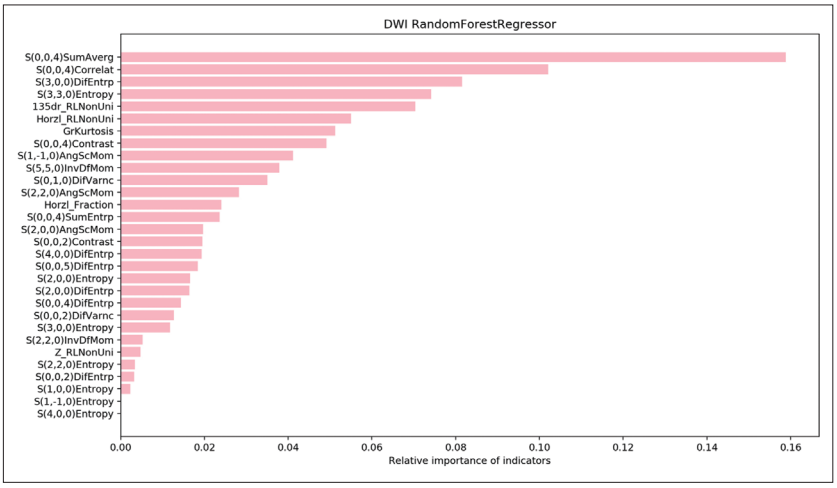

B

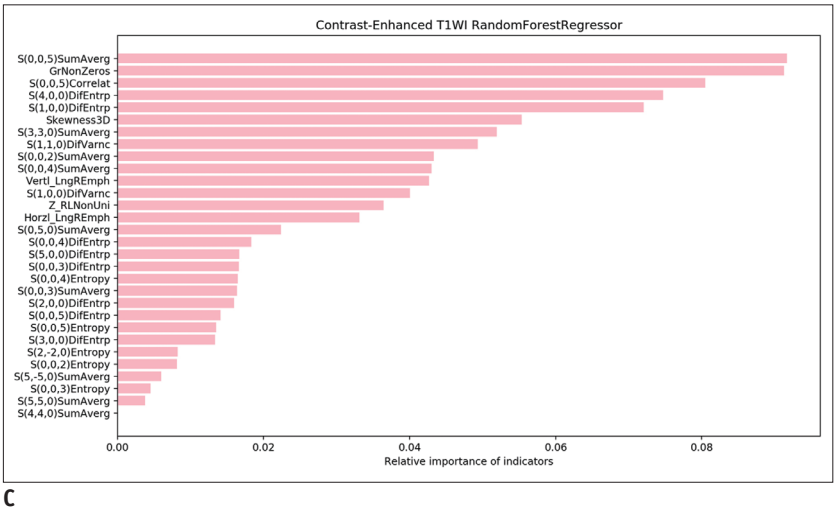

C

Fig. 5. The relative importance of the 30 optimal texture features derived from T2WI (A), DWI (B), and CE-MRI images (C) were automatically calculated using the Random Forest model. AngScMom = angular second moment, Correlat = correlation, DifEntrp = difference entropy, DifVarnc = difference variance, GrKurtosis = absolute gradient kurtosis, GrNonZeros = percentage of pixels with nonzero gradient, GrSkewness = absolute gradient skewness, GrVariance = absolute gradient variance, Horzl_Fraction = horizontal_fraction of image in runs, Horzl_RLNonUni = horizontal_run length nonuniformity, InvDfMom = inverse difference moment, LngREmph = long run emphsis, SumAverg = sum average, SumOfSqs = sum of suqares, SumVarnc = sum variance, Vertl_ShrtREmp = vertical_short run emphsis, 135dr_RLNonUni = 135 degree_run length nonuniformity, 135dr_ShrtREmp = 135 degree_short run emphsis

https://doi.org/10.3348/kjr.2020.0121

Korean Journal of Radiology
KJR

Table 5. Diagnostic Performance of the Non-Texture Model and Combined Model in Differentiating BEOTs from MEOTs

Moden	Training Group (n = 62)					Test Group (n = 26)			
	*P**	Se (%)	Sp (%)	Ac (%)	AUC	Se (%)	Sp (%)	Ac (%)	AUC
Non-texture model	< 0.001	78.3	84.6	82.3	0.818	73.3	90.1	80.8	0.840
Combined model	< 0.001	92.5	86.4	90.3	0.962	75.0	94.0	88.5	0.896

*Omnibus Tests of Model Coefficients. Ac = accuracy, AUC = area under the receiver operating characteristic curve, Se = sensitivity, Sp = specificity

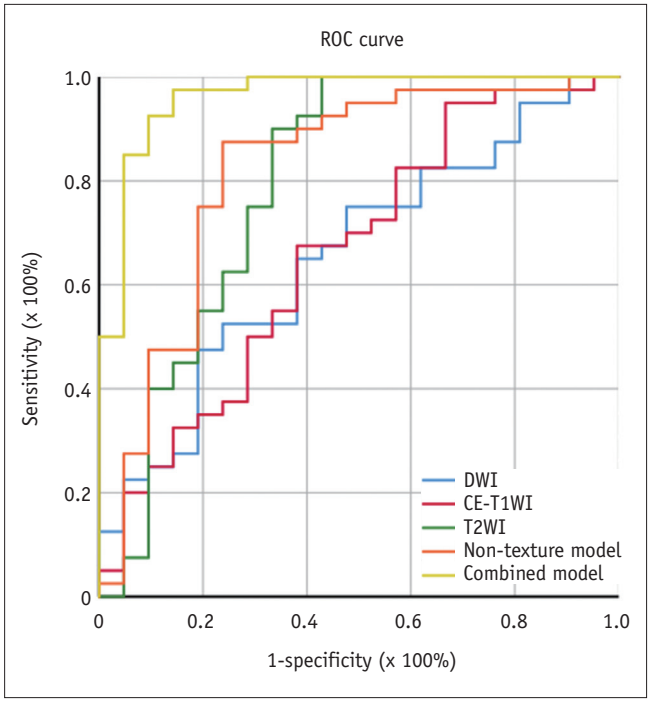

Fig. 6. ROC curves of the logistic models and single texture features of BEOTs and MEOTs in the training group. The AUCs of the most weighted texture feature extracted from CE-T1WI, DWI, and T2WI images are 0.690, 0.728, and 0.818, respectively. The AUC of the non-texture model is 0.818 and that of the combined model is 0.962. AUC = area under the ROC curve, ROC = receiver operating characteristic

the combined model and single texture feature approaches showed that the combined model outperformed any single texture feature, including the S(0,1,0) DifEntrp (AUC, 0.818; 95% CI, 0.699–0.904, $p = 0.020$), S(0,0,4) SumAverg (AUC, 0.728; 95% CI, 0.600–0.833, $p < 0.001$), and S(0,0,5) SumAverg (AUC, 0.690; 95% CI, 0.560–0.801, $p < 0.001$) in the training group.

DISCUSSION

This study assessed the diagnostic performance of texture analysis in the discrimination of BEOTs from FIGO stage I/II MEOTs. Our results showed that texture features derived from T2WI, DWI, and CE-T1WI images significantly differed between the BEOT and MEOT groups. In addition, diagnostic models that combine texture features and conventional variables could accurately differentiate BEOTs from MEOTs.

It has become acceptable to perform conservative fertility-sparing surgery and to omit lymphadenectomy during the treatment of BEOTs due to their favorable prognosis, while conservative surgery is restricted to only stage I A serous, mucinous, or endometrioid MEOTs (18). Imaging analyses of stage III or higher MEOTs tend to reveal a more aggressive appearance (obvious lymphatic spread and distant metastasis), and an ovarian tumor with such features can be easily diagnosed as an MEOT. On the other hand, a considerable portion of stage II MEOTs with pathologically confirmed pelvic invasion cannot be seen with the naked eye. Thus, we recruited only stage I/II MEOTs patients for this study. Our results demonstrated that either a mixed cystic/solid or predominantly-solid configuration and a greater solid component were more frequently found in stage I/II MEOTs. These findings are consistent with previous observations (19, 26).

Texture analysis is a novel imaging technique that can extract extensive data from biomedical images and can be investigated with textural analysis tools. Texture analysis of MRI images is performed by analyzing the gray tone variations among image voxels. This method captures spatial and intensity information that identify pathological changes and microstructural heterogeneity within a tumor. Since the voxel size in the MR images in this study was 1 mm and the features of texture analysis were set to no less than 6 bits per voxel for texture extraction, the texture features detected subtle differences between MR images of BEOTs and MEOTs. Due to the heterogeneity of ovarian tumors, texture features based on the whole tumor contained more spatial information (along the extra-dimension) and higher sensitivity and specificity than traditional techniques which are based on a pre-selected region of interest.

In our study, single texture features extracted from T2WI, DWI, and CE-T1WI images were significantly different between BEOTs and MEOTs. Considering that the same acquisition conditions were used, this might be due to the essential differences in spatial and intensity characteristics

https://doi.org/10.3348/kjr.2020.0121

among image voxels caused by pathological changes and microstructural heterogeneity within different tumors. However, the single texture feature of CE-T1WI (AUC, 0.690) and DWI (AUC, 0.728) images showed a relatively lower diagnostic performance in the training group compared to that of T2WI images (AUC, 0.818). On CE-T1WI images, the difference in radiologic features between BEOTs and MEOTs may be related to the limitation of CE images, which are not sufficient to identify changes in the microcirculation induced by neoangiogenesis. This is consistent with our conventional imaging findings (p = 0.691) and several previous studies (10, 11, 19). On DWI images, this may be associated with the lower signal-to-noise ratio and the lack of ADC mapping.

Our results also indicated that the combined model showed the highest diagnostic performance in differentiating BEOTs from MEOTs, when compared to the non-texture model and the single texture features. This combined model used in the training group (accuracy, 90.3%) was validated in the test group (accuracy, 88.5%) and there was no significant difference in the combined model between the two groups (p = 0.348). However, the superiority of the combined model compared to the non-texture model was not significant in the test group. The predictability of diagnostic models tend to be higher in the training group than in the test group (27). This may result in decreased differences between the combined model and non-texture model in a test group. This reduced predictability may also be due to the complexity of the combined model (three texture features were added) for the training group compared to the non-texture model, leading to the impaired generalization capability of the model and the decreased accuracy of the combined model in the test group. Moreover, the increased number of variables in the combined model are more likely to result in an over-fitting phenomenon due to the small sample size in the test group.

This study still had several limitations. First, due to its retrospective design and relatively small sample size, it was impossible to compare different histological tumor types, limiting the generalizability and statistical power of the study. Second, our study only separated samples into either the training or test group in order to perform internal validation; however, external validation is still required. Therefore, further multi-center studies with larger patient sample sizes are needed to validate the applicability of our findings. Finally, although this study described preliminary results on texture analysis of MR images for the differentiation of BEOTs from MEOTs, further studies are needed to investigate the pathological basis of our findings.

In conclusion, MRI-based texture analysis of the whole tumor may assist in characterizing the differences between BEOT and MEOT patients. These findings in turn may guide diagnostic protocols for future patients. Furthermore, MRI texture features combined with clinical and conventional MRI characteristics exhibit better diagnostic performance than texture features alone.

Conflicts of Interest

The authors have no potential conflicts of interest to disclose.

Acknowledgments

The authors thank the radiographers in our departments for their assistance in the experimental studies as well as data analysis.

ORCID iDs

Rongping Ye
https://orcid.org/0000-0001-7867-9752
Shuping Weng
https://orcid.org/0000-0001-8271-934X
Yueming Li
https://orcid.org/0000-0002-3669-568X
Chuan Yan
https://orcid.org/0000-0003-4106-8995
Jianwei Chen
https://orcid.org/0000-0002-5791-9865
Yuemin Zhu
https://orcid.org/0000-0001-9630-0160
Liting Wen
https://orcid.org/0000-0002-3009-8630

REFERENCES

1. Lalwani N, Prasad SR, Vikram R, Shanbhogue AK, Huettner PC, Fasih N. Histologic, molecular, and cytogenetic features of ovarian cancers: implications for diagnosis and treatment. *Radiographics* 2011;31:625-646
2. Kurman RJ, Carcangiu ML, Herrington CS, Young RH. *WHO classification of tumors of female reproductive organs*, 4th ed. Lyon: International Agency for Research on Cancer, 2014
3. National Comprehensive Cancer Network. *Ovarian cancer including fallopian tube cancer and primary peritoneal cancer (Version 1.2020)*. Philadelphia: National Comprehensive

https://doi.org/10.3348/kjr.2020.0121

Cancer Network, 2020
4. Bentivegna E, Gouy S, Maulard A, Pautier P, Leary A, Colombo N, et al. Fertility-sparing surgery in epithelial ovarian cancer: a systematic review of oncological issues. *Ann Oncol* 2016;27:1994-2004
5. Vasconcelos I, de Sousa Mendes M. Conservative surgery in ovarian borderline tumours: a meta-analysis with emphasis on recurrence risk. *Eur J Cancer* 2015;51:620-631
6. Naqvi J, Nagaraju E, Ahmad S. MRI appearances of pure epithelial papillary serous borderline ovarian tumours. *Clin Radiol* 2015;70:424-432
7. Sherman ME, Mink PJ, Curtis R, Cote TR, Brooks S, Hartge P, et al. Survival among women with borderline ovarian tumors and ovarian carcinoma: a population-based analysis. *Cancer* 2004;100:1045-1052
8. Bazot M, Haouy D, Daraï E, Cortez A, Dechoux-Vodovar S, Thomassin-Naggara I. Is MRI a useful tool to distinguish between serous and mucinous borderline ovarian tumours? *Clin Radiol* 2013;68:e1-e8
9. Bent CL, Sahdev A, Rockall AG, Singh N, Sohaib SA, Reznek RH. MRI appearances of borderline ovarian tumours. *Clin Radiol* 2009;64:430-438
10. Takemori M, Nishimura R, Hasegawa K. Clinical evaluation of MRI in the diagnosis of borderline ovarian tumors. *Acta Obstet Gynecol Scand* 2002;81:157-161
11. deSouza NM, O'Neill R, McIndoe GA, Dina R, Soutter WP. Borderline tumors of the ovary: CT and MRI features and tumor markers in differentiation from stage I disease. *AJR Am J Roentgenol* 2005;184:999-1003
12. Thomassin-Naggara I, Daraï E, Cuenod CA, Rouzier R, Callard P, Bazot M. Dynamic contrast-enhanced magnetic resonance imaging: a useful tool for characterizing ovarian epithelial tumors. *J Magn Reson Imaging* 2008;28:111-120
13. Zhao SH, Qiang JW, Zhang GF, Ma FH, Cai SQ, Li HM, et al. Diffusion-weighted MR imaging for differentiating borderline from malignant epithelial tumours of the ovary: pathological correlation. *Eur Radiol* 2014;24:2292-2299
14. Lu J, Pi S, Ma FH, Zhao SH, Li HM, Cai SL, et al. Value of normalized apparent diffusion coefficients in differentiating between borderline and malignant epithelial ovarian tumors. *Eur J Radiol* 2019;118:44-50
15. Han X, Sun M, Wang M, Fan R, Chen D, Xie L, et al. The enhanced T2 star weighted angiography (ESWAN) value for differentiating borderline from malignant epithelial ovarian tumors. *Eur J Radiol* 2019;118:187-193
16. Incoronato M, Aiello M, Infante T, Cavaliere C, Grimaldi AM, Mirabelli P, et al. Radiogenomic analysis of oncological data: a technical survey. *Int J Mol Sci* 2017;18:805
17. Ng F, Kozarski R, Ganeshan B, Goh V. Assessment of tumor heterogeneity by CT texture analysis: can the largest cross-sectional area be used as an alternative to whole tumor analysis? *Eur J Radiol* 2013;82:342-348
18. Denewar FA, Takeuchi M, Urano M, Kamishima Y, Kawai T, Takahashi N, et al. Multiparametric MRI for differentiation of borderline ovarian tumors from stage I malignant epithelial ovarian tumors using multivariate logistic regression analysis. *Eur J Radiol* 2017;91:116-123
19. Li YA, Qiang JW, Ma FH, Li HM, Zhao SH. MRI features and score for differentiating borderline from malignant epithelial ovarian tumors. *Eur J Radiol* 2018;98:136-142
20. Thomassin-Naggara I, Aubert E, Rockall A, Jalaguier-Coudray A, Rouzier R, Daraï E, et al. Adnexal masses: development and preliminary validation of an MR imaging scoring system. *Radiology* 2013;267:432-443
21. Ma FH, Zhao SH, Qiang JW, Zhang GF, Wang XZ, Wang L. MRI appearances of mucinous borderline ovarian tumors: pathological correlation. *J Magn Reson Imaging* 2014;40:745-751
22. Szczypiński PM, Strzelecki M, Materka A, Klepaczko A. MaZda--a software package for image texture analysis. *Comput Methods Programs Biomed* 2009;94:66-76
23. Strzelecki M, Szczypinski P, Materka A, Klepaczko A. A software tool for automatic classification and segmentation of 2D/3D medical images. *Nucl Instrum Methods Phys Res A* 2013;702:137-140
24. Szczypinski PM, Strzelecki M, Materka A. *MaZda-A software for texture analysis*. 2007 international symposium on information technology convergence (ISITC 2007);2007 November 23-24; Jeonju, Korea
25. Tourassi GD, Frederick ED, Markey MK, Floyd CE Jr. Application of the mutual information criterion for feature selection in computer-aided diagnosis. *Med Phys* 2001;28:2394-2402
26. Kurata Y, Kido A, Moribata Y, Kameyama K, Himoto Y, Minamiguchi S, et al. Diagnostic performance of MR imaging findings and quantitative values in the differentiation of seromucinous borderline tumour from endometriosis-related malignant ovarian tumour. *Eur Radiol* 2017;27:1695-1703
27. Iasonos A, Schrag D, Raj GV, Panageas KS. How to build and interpret a nomogram for cancer prognosis. *J Clin Oncol* 2008;26:1364-1370